Regional Evolution of the Meteosat Solar and Infrared Spectra (2005-2024) Linked to Cloud Cover and Ocean Surface

José I. Prieto-Fernández and Humberto A. Barbosa *

Posted Date: 24 February 2026

doi: 10.20944/preprints202510.2286.v2

Keywords: satellite observations; radiance; absorption of thermal radiation; radiation flux; long-term series

 doi:10.20944/preprints202510.2286.v2

Article

Regional Evolution of the Meteosat Solar and Infrared Spectra (2005-2024) Linked to Cloud Cover and Ocean Surface

José I. Prieto-Fernández [1] and Humberto A. Barbosa [2,*]

[1] PraproSL, Castuera, Spainm

[2] Satellite Image Processing and Analysis Laboratory (LAPIS), Federal University of Alagoas (UFAL), A C Simões Campus, Maceió 57072-900, Brazil

* Correspondence: humberto.barbosa@icat.ufal.br; Tel.: +558 299 999 3043

Abstract

In this paper we analyze the evolution of atmospheric and surface physical properties on that portion of the Earth covered by the Meteosat Second Generation (MSG) satellites over a period of 20 years (from 2005 to 2024). The radiances show significant changes over time in the solar (–1.3 %) and infrared (+0.4%) domains, consistent with data from similar radiometers (e.g. CERES) on other satellite platforms. The outgoing solar radiance (OSR) mainly decreases as a result of low-level cloud reduction in the nominal Meteosat (at 0° longitude) field of view (MFoV) in the geostationary orbit. The increased CO_2 content in the atmosphere also plays a decisive role in the radiation imbalance at the top of the atmosphere (ToA). For 60 MFoV subareas we describe regional changes in the cloud amount at high and low levels in the atmosphere, and show the connection between the imbalance at the ToA and the observed variation in the sea surface temperature (SST) in the Atlantic. We also did not find any significant cirrus variation in the study period. Our study provides a better spectral resolution in its conclusions compared with other analyses, such as those of CERES. It also introduces the SST as a major representative of the climate. For example, the radiance values in the atmospheric split window measurements around 11 μm can be used as a proxy for the humidity column at low levels, a key variable in climate projections, which shows a decadal increase. Meteosat data suggests a so-far unpredictable contribution to climate from the deep ocean and its heat reserve. The recent decrease in the total cloud cover (TCC) at low levels in the MFoV is also validated by the ECMWF ERA-5 reanalysis.

Keywords: satellite observations; radiance; absorption of thermal radiation; radiation flux; long-term series

1. Introduction

Meteorological satellite measurements sample the spectrum of the radiation reflected or emitted by the Earth. Key variables are cloudiness and the concentration of absorbing gases plus aerosols. These variables determine the surface temperature and steer the Earth's radiative balance [1].

Changes in that balance, due to natural climate variability and human activity, translate to surface warming and adopt diverse regional patterns. Products and datasets from low-Earth-orbit [2] and geostationary [3,4] satellites are used to derive the components of the Earth Radiation Budget (ERB) at the top of the atmosphere (ToA), recognized as one of the Essential Climate Variables [5]. Meteosat Second Generation (MSG) is a European geostationary satellite system now replaced by an improved third generation. Since 2004 MSG has provided temporal samples at 15-minute intervals that capture information about the radiation crossing the ToA [6,7,8].

Accurate Meteosat calibration is a prerequisite for using its data for climate analysis. This has been achieved by inter-calibration of the Spinning Enhanced Visible and Infrared Imager (SEVIRI)

 doi:10.20944/preprints202510.2286.v2

with the polar-orbiting imager MODIS (on the Aqua satellite). The inter-calibration relies on regressions of collocated near-nadir reflectances, corrected for differences in spectral response between instruments [9]. "The SEVIRI operational calibration is found to be stable [..] and robust for a range of choices regarding data collocation and [..] the viewing and illumination geometries of the two instruments." The differences in brightness temperatures are in the order of 0.1 K for most channels, but almost 1 K for the CO_2 absorption channel at 13.4 μm, which is occasionally affected by icing [10]. We will use here the similarity with results from other radiation budget studies like those on CERES or ERA-5 (ECMWF) as the main validation or confirmation of our findings [15].

A review paper [11] summarizing the advances in the utilization of radiation measurements explores the direct use of spectral observations to evaluate climate models. The evolution of the outgoing longwave radiation (OLR) in the Meteosat radiance measurements is somewhat surprising. A warmer surface is expected to produce a corresponding increase in OLR, as expressed by the Stefan-Boltzmann law, but this is not evident for the total of non-solar Meteosat channels, which only show a very slow growth in time. At least a part of the explanation for the present surface warming must lie then in the solar domain [12].

As an extension of a previous work by the authors [13] we explore now the regional variability in the ToA imbalance and its connection with the sea surface temperature (SST) in the Atlantic and west Indian oceans, based on radiance fluxes measured by Meteosat over the period 2005–2024.

The Intergovernmental Panel on Climate Change (IPCC, AR5) expresses doubt about the cloud feedback [14]: "Low clouds contribute positive feedback in most models, but that behavior is not well understood." Here we try to show the relevance of the decrease in low cloud to the global warming of the last few decades, as supported purely by satellite data. Satellites are not good at discriminating low and high cloud, but we hope that the regional separate analysis of the MFoV clarifies the importance of the low cloud evolution.

2. Data and Methods

The method used in this study is described in a previous work [13], here upgraded and applied to a longer time period. The use of a longer data series is more representative of the recent climate, and has reduced the uncertainty of the results by 45%. Each complete set of measurements of the whole Meteosat Field of View (MFoV) on an operational cycle of 15 minutes is considered a 'slot'. We compare slot and channel average radiances for an initial period of time ('ancient', from January 2005 to December 2014) with radiances for a final period ('recent', from January 2015 to December 2024), to determine data trends in ten years. See Table 1.

The SEVIRI radiometer on board MSG scans the MFOV at eleven different wavelengths, with sub-satellite point horizontal resolution of 3 km × 3 km. The achieved data resolution is better than ±0.1 K for brightness temperatures as a result of data grouping in 4 × 4 pixel boxes.

Data differences are built with a lag of 522 weeks, approximately ten years. For example, we compare the MFOV average data in the Meteosat slot at the nominal date and time Friday 7 January 2005 at 12 00 UTC with the slot on Friday 9 January 2015 at 12 00 UTC, and so on for subsequent pairs of slots. Based on all pairs separated by approximately ten years, we build a good estimate of the change of slot-averaged radiances in the eleven Meteosat SEVIRI channels. We choose a constant weekday for all the slot comparisons to avoid possible minor changes in the images due to different human activities on different weekdays. This weekly choice, rather than a more frequent data sampling, proves robust, since a week is a typical decoupling time for satellite images as concerns the autocorrelation function (Pearson correlation ~0.48).

We define the terms radiance and flux in this paper as follows. **Radiance** (in units $mW{\cdot}m^{-2}{\cdot}sr^{-1}{\cdot}(cm^{-1})^{-1}$, where *mW* stands for milliwatt, *m* for meter and *sr* for steradian, the solid angle unit. We refer to that radiance unit in the figures as SRU, standard radiance unit) is the power per surface unit, per steradian and per wavenumber unit. **Flux** (in $W{\cdot}m^{-2}$ units), also named **integrated radiance** or irradiance, is the result of integrating in the spectral domain, and in solid angle (by using the factor π), the radiance measured by the satellite.

 doi:10.20944/preprints202510.2286.v2

As an example, Figure 1 shows the slot-averaged **radiance** around 0.6 μm measured by Meteosat. Radiance values oscillate between 3.2 SRU around June-July, the less cloudy period in the year, and 4.6 SRU around the equinoxes. Dots with the differences in ten years (Figure 1a) form a cluster biased to a negative value around –0.1 SRU, indicating a decrease of reflected radiation, plausably corresponding to a significant decrease in cloud cover for all seasons. In the scatter plot in (a), the months of June and July present the lowest average reflectivity in the year. Cloud loss in a decade is however similar for all times in the year. The scatter plot in (b) relates average reflectivity to the contrast (standard deviation) in the satellite image, higher in the presence of abundant cloud, as is the case around equinoxes.

The time series (in c and d, before and after de-seasonalizing) shows a clear statistical trend, and all values in (d) in the decade 2015-2024 for 0.6μm radiances are below those ten years before. This result coincides with the results for CERES [15].

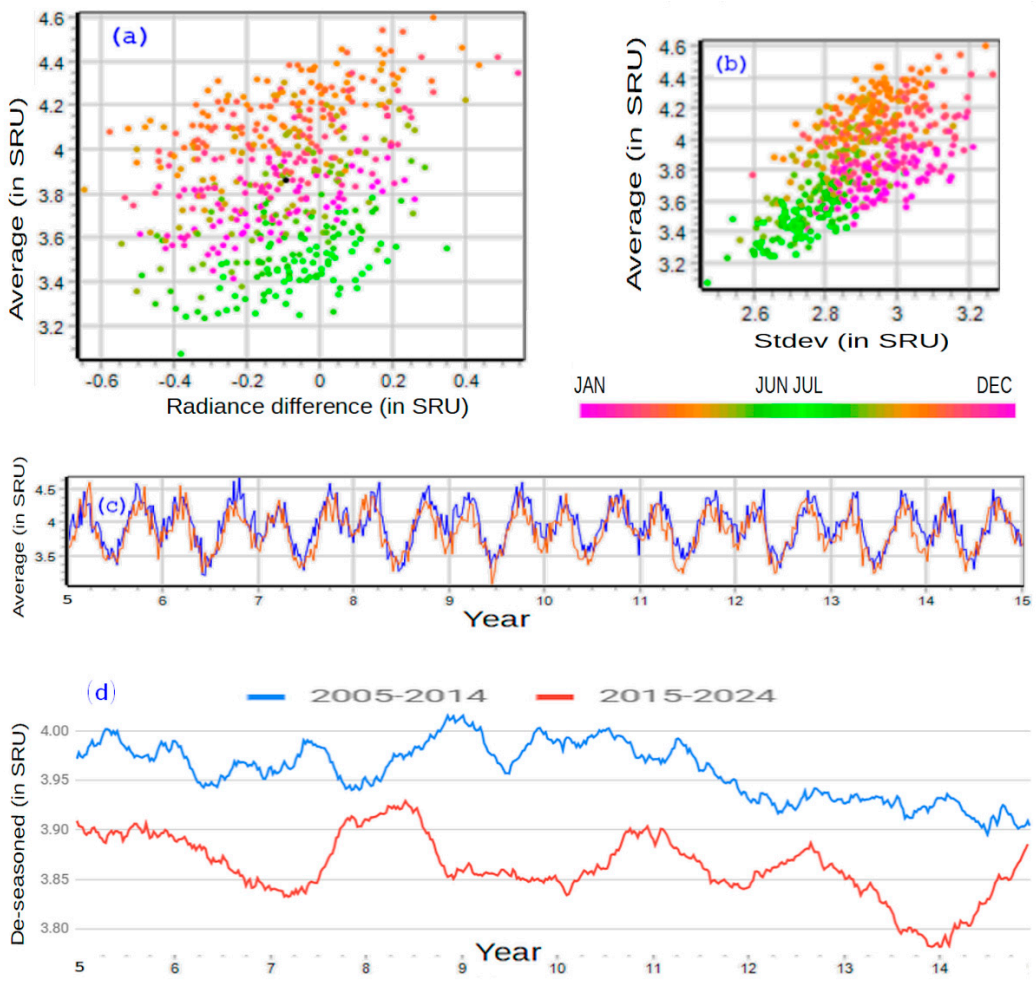

Figure 1. Evolution of average radiance values measured on channel 0.6 μm of Meteosat. (**a**) Scatter plot of differences in the slot averages (horizontal axis) for slots separated by precisely 10 years ±2 days, compared with the 'recent' slot average (vertical axis) of that difference, showing a significant radiance reduction in a decade (black dot is the distribution center of mass). (**b**) Scatter plot for the connection between 'recent' slot average values (vertical) and standard deviation inside the slot (horizontal, a measure of pixel radiance uniformity and a proxy for cloud amount in the scene). Dot colors for (a) and (b) indicate month of the year, with highest values showing around the equinoxes. (**c**) Comparison of reflected radiance values at 0.6μm for a time lapse of ten years: brown line for 'recent' and blue line for 'ancient' radiance, the 'recent' typically higher in value. The yearly cycle of radiance shows two high peaks around the equinoxes in the MFoV. (**d**) Same as in c, after deseasonalizing the series, to mark the most critical moments in the evolution of solar radiance around 0.6 μm.

 doi:10.20944/preprints202510.2286.v2

For confirmation that this is not linked to calibration artifacts, we found in the ERA-5 database of atmospheric reanalysis a parallel evolution of the total cloud cover ('TCC') averaged for the area between geographical latitudes=(–50°,50°) and longitudes=(–70°, 70°), with a Pearson correlation between the two series of 0.71, which indicates a reassuring agreement with an external reference (Figure 1.2). Recent trend discrepancies remain unexplained, but will hopefully be clarified when fresh data from 2025 and 2026 are added to the study.

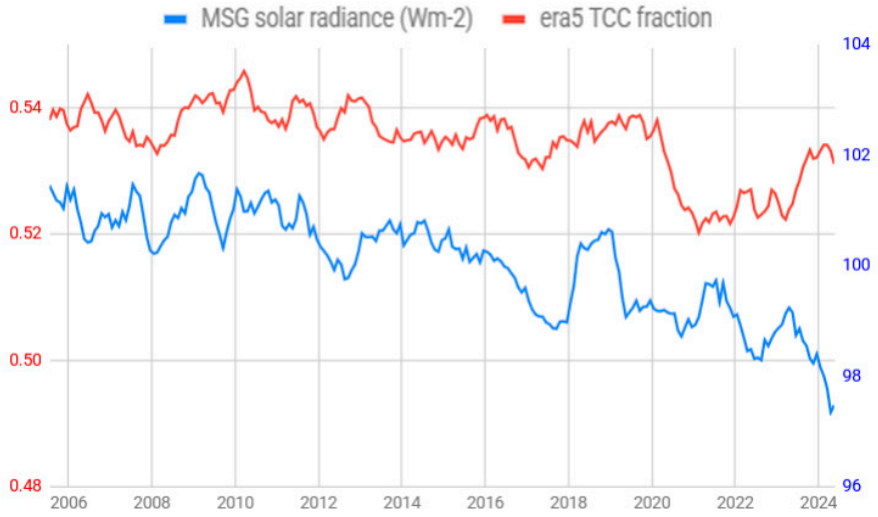

Figure 1.2. Temporal comparison of integrated solar reflected radiances in the MFoV, and the ERA-5 total cloud cover for the area latitude=(–50°,50°) and longitude=(–70°, 70°). The series were de-seasonalized. Expected discrepancies due to cloud type and phase do not blur the time downward trend in both magnitudes, with a Pearson correlation of 0.71. Radiances (in blue) are expressed in Wm^{-2}. Their time series allows a direct comparison with the total cloud cover fraction from ERA-5.

A note on image similarity: slots separated by **24 hours** show typical Pearson correlation coefficients of 0.95 ± 0.02, but only 0.48 ± 0.05 if the two images are separated by **one week**. If we compare monthly image **averages** for consecutive months, where the rapid movement of cloud is averaged out, the correlation grows to 0.71 ± 0.03. Longer period averages increase the correlation, i.e., an averaged year is very similar to the next averaged year. And for longer averages, the 0.6 μm solar correlation between 10-year averages of 0.6μm solar images reaches 0.994.

Table 1. Data set composition (European dates format).

Meteosat dataset	points	periodicity	start date	end date
ancient	522	weekly	31.12.2004	26.12.2014
recent	522	weekly	02.01.2015	27.12.2024

On an initial (ancient) and a final (recent) period, each ten years long (3647 days or 521 weeks) consisting of 522 slots, we attain statistical significance for most channels.

We use the 522 pairs of slots for three kinds of statistical analyses: (a) MFoV pixel average for each channel used to estimate trends, in Figure 2. (b) Local change of pixel averages for all pixels, shown in Figure 3 for two of the channels. (c) Pixel sampling for inter-channel comparisons in Figure 4.

The characteristics of the SEVIRI channels are shown in the first four columns of Table 2. The information from Meteosat is available at the EUMETSAT data portal https://user.eumetsat.int (free registration is required to access data). We extracted calibrated and rectified (level 1.5) radiances from December 2004 to December 2024 at 12 UTC in the MFOV from the satellite at 0° longitude. Data are retrieved as files with a count value for each pixel, channel and nominal time. The count value is

 doi:10.20944/preprints202510.2286.v2

converted into spectral radiance units (SRU) with the help of the slot calibration coefficients in each retrieved file. In this study, we restrict ourselves to the slot labeled 12 UTC, which contains MFOV data captured between 1200 UTC and 1212 UTC, acquired from south to north, roughly corresponding to midday conditions at the Greenwich meridian. The trends estimated in this study (defined here as the change between the final and initial measurements) are the differences in slot-average values measured with a 10 year interval on the 11 different channels of SEVIRI (see Table 2).

For the interpretation of the atmospheric and ground evolution, we group Meteosat SEVIRI channels in four spectral categories (last column in Table 2 and Figure 2), which requires the integration of the measurements in solid angle. In the Lambertian hypothesis for radiative emission from a surface, channels get divided by a correction constant π to compensate for null values in the night. We encounter a limitation in how well the channels represent the spectral domain. As seen in the 4th column of Table 2, the bandwidths in SEVIRI channels partially overlap and do not completely cover the infrared or solar domain. The channel grouping therefore introduces errors of ±0.15 Wm^{-2} for each group of integrated radiances (last column in Table 2). That error estimate results from a Monte-Carlo approach on different choices of boundary values between the individual channels.

Table 2. Characteristics of Meteosat SEVIRI channels (labeled from 1 to 11) in columns 1 to 4. Estimates of average values of the spectral radiance (5th column) per channel. Wavenumber-integrated values (in Wm^{-2}) within the channel interval in the 6th column). Integrated radiance variation in 10 years (spectral values for the average difference of the observed pairs, in the 7th column. The 8th (last) column groups the integrated variations by spectral region, from the 7th column.

Domain	Meteosat Channel	Central Wavelength μm	Channel boundaries μm	Spectral radiance (in SPU) 10^{-3} Wm^{-2} sr^{-1} $(cm^{-1})^{-1}$	Integrated radiance Wm^{-2}	10-year change by channel Wm^{-2}	Change by domain Wm^{-2}
solar	1	0.64	0.56—0.71	3.91	22.7	–0.56	
solar	2	0.81	0.74—0.88	4.99	41.1	–0.42	sum solar = –1.07
solar	3	1.64	1.50—1.78	4.01	33.5	–0.10	(channels 1-4)
solar+infrared	4	3.92	3.48—4.36	0.83	3.2	0.01	
water vapor	5	6.25	5.35—7.15	3.29	10.6	0.14	sum WV = 0.11
water vapor	6	7.35	6.85—7.85	14.32	17.4	–0.03	(5-6)
infrared window	7	8.7	8.30—9.10	51.72	45.4	0.30	
infrared ozone	8	9.66	9.38—9.94	43.82	26.5	0.11	sum IR = 0.76
infrared window	9	10.8	9.80—11.80	86.80	47.3	0.25	(7-10)
infrared window	10	12.0	11.00—13.00	98.46	47.8	0.10	
CO_2 absorption	11	13.4	12.40—14.40	80.37	45.2	–0.58	CO_2 = –0.58 (11)

We integrate in the spectral domain and angular domain to obtain radiances (in units Wm^{-2}) through the formula:

$$Radiance\ variation = Const * Spectral\ radiance\ variation * Channel\ spacing \quad (1)$$

with *Const* = 1 for solar channels (numbers 1 to 4) and *Const* = π for infrared channels (from 5 to 11). The value (*Const*=1) produces a 24-hour average out of the measured day data at 12 UTC, assuming a typical cycle of 12 night hours 12 hours of day illuminations described by a positive sine function. *Channel spacing* is the width assigned to each channel in order to cover up the infrared spectral region while minimizing the inter-decadal channel variations.

The climate is driven by (a) the net amount of radiation entering and leaving the Earth-atmosphere at its top, consisting of the Earth's reflected shortwave radiation (RSW) and the Outgoing Longwave Radiation (OLR), plus (b) the heat absorbed or emitted by the deep oceans and, to a lesser extent, by the subsoil [16]. The former two quantities, RSW and OLR, can be respectively assessed from Meteosat solar channels (1 to 4) and infrared channels (5 to 11). The solar incoming radiation (SIR) varies with the Earth-Sun distance in the course of the year. See [17] for details.

As an equation for the climate imbalance (we call it CI here, but often it is also referred as Earth Energy Imbalance, EEI) we use:

 doi:10.20944/preprints202510.2286.v2

$$CI = SIR - RSW - OLR \quad (2)$$

This imbalance translates into the Earth surface temperature change, with a growing trend in recent decades [18], plus the heat storage in the ocean and inner land layers. From the satellite perspective in formula (2), any reduction in the satellite measured radiances (exiting the planet) means an increase of the imbalance, CI. We admit a limitation in the accuracy of the method beyond 14 μm, since no Meteosat channel covers that spectral region. We use a simple extrapolation for it based on the values from channel 11 of SEVIRI.

A summary of strengths and limitations in this study is presented in Table 3.

Table 3. Qualitative evaluation of the data and methods used in the study.

Aspect	Strength	Limitation
Source radiance data (SEVIRI)	High radiance accuracy after calibration and inter-calibration	Only for Meteosat field of view, not whole world surface
Spectral integration	More accuracy gained through averaging	Poor representation of SEVIRI channels in parts of the spectrum, e.g., above 15 μm
Radiation Transfer simulation	Calibration based in CO_2 concentrations from other reliable sources	Disregards cross absorption effects by several gases
Temporal data sampling	Large weekly independence, ENSO-Niño neutral on averages of two periods	Potentially exposed to multi-year anomalies in the large MFoV region. No consideration of night slots or conditions
Connection to climate	Immediate connection of satellite radiances to climate variables, cloud and gas	Too short a period (20 years) for sound climate conclusions or sustained trends
Contribution to similar studies	Conclusions based on a wider spectral basis than in other studies (e.g. Loeb [15])	Discrepancies on the cloud evolution and fluctuation compared with other studies
Future analyses	Easy translation to sub-regional trends in brightness temperatures	Geographical coverage limited to MFoV, requiring extra use of polar satellites (LEO) for a global analysis

3. Results

3.1. MFoV Analysis

Figure 2 summarizes the spectrally integrated per-decade variation (in Wm^{-2}) for the eleven MSG channels, by comparing the 'recent' 10-year period (2015–2024, in blue) with the 'ancient' period 2005-2014.

 doi:10.20944/preprints202510.2286.v2

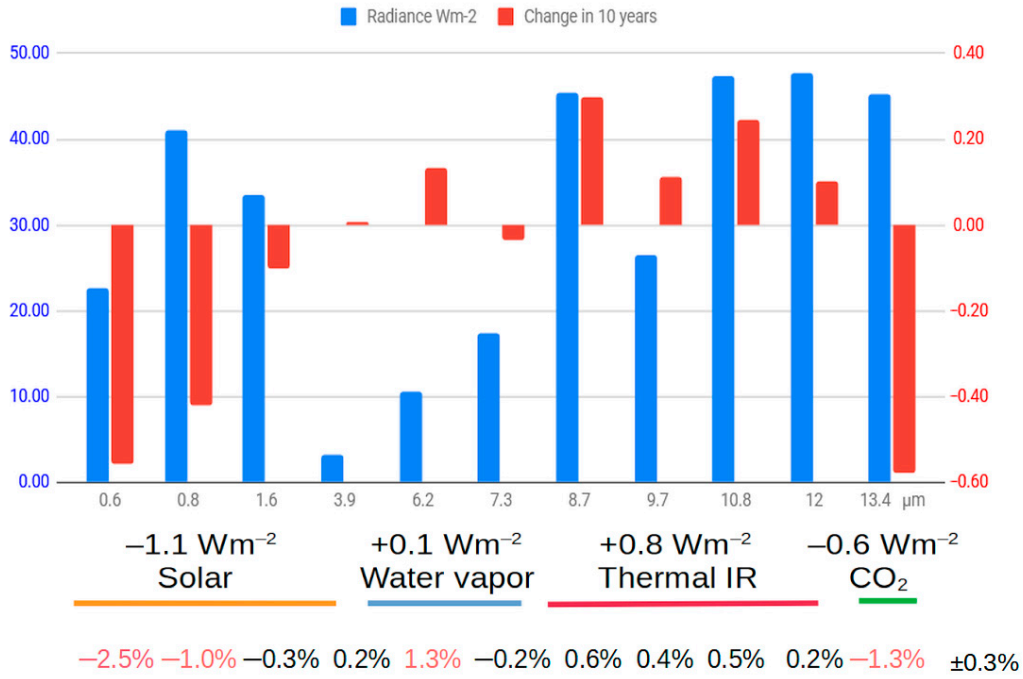

Figure 2. Decadal radiance average and change in the period 2005 to 2024 for the eleven MSG channels, as defined in Table 2, in Wm^{-2}. Blue bars indicate the integrated radiance around the central wavelength. Red bars show the decadal change. Labels under the diagram are sums of the 10-year variation in Wm^{-2} for the solar, water vapor, infrared and CO_2 absorption spectral regions. Percentages in the bottom line are marked in red for statistically significant channel changes above 1%.

We take the central wavenumbers of the MSG channels as the basis for the channel interval width estimation, and integrate in stereo angle and wavenumber. Excepting those at 7.3 μm and at 12 μm, the channels show statistically significant variations in the radiance per unit of wavenumber (usually expressed in cm^{-1}).

For the solar channels (SEVIRI channels 1 to 4) and for the CO_2 channel (SEVIRI channel at 13.4 μm) a negative radiance trend is observed. The radiances can be grouped in four regions by wavelength as seen in Figure 2, labeled: solar, water vapor, thermal infrared and CO_2 spectral domains. The radiance changes in Wm^{-2} for the four groups, with uncertainties of ±0.15 Wm^{-2}, are also indicated. Most outstanding variations occur for channels centered at 0.6, 0.8, 6.2 and 13.4 μm. These results were already analyzed and commented in [13] and highlight the primary role of cloud in the flux balance at the ToA. The OLR around 0.2 Wm^{-2} for a decadal recent warming around 0.2 K is short compared with the hypothesis of linearity for the OLR on the surface temperature [19]: "The longwave clear-sky (LWCS) feedback has diverse spatial patterns in CMIP5 models, yet the global-mean feedback is robustly 1.9 W/m2/K".

The outgoing radiance decrease in the CO_2 absorption region appears to be the consequence of the continuously increasing gas level, currently at a rate of about 6% per decade. The radiance decrease at channel 13.4 μm can be explained by that increase compounded with an increase in air temperature of (0.34 ± 0.08) K/decade. A similar air warming could also explain the measured increase at channel 5 around 6.2 μm. However, de-icing around the water vapor and CO_2 sensors in SEVIRI could also affect this channel accuracy. Anyway, water vapor channels have a limited impact on the radiance balance, since they monitor a spectral region with low OLR. See Figure 2 for a comparison with other regions. The atmosphere specific humidity likely changed in ways we try to ascertain from channels at 10.8 μm and 12 μm [20], whose difference grows in every sub-region of the MFoV. See Figure 4 (bottom image).

 doi:10.20944/preprints202510.2286.v2

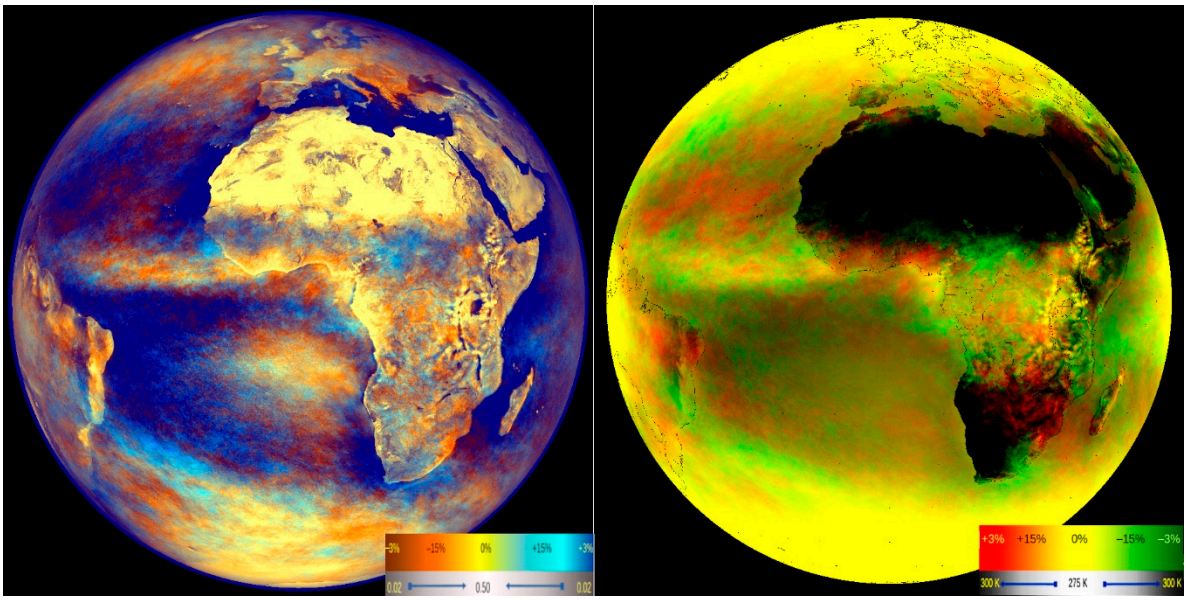

Figure 3. Decadal trend in percentage according to the color scale. (**Left**, for channel 0.6 μm) Orange hues indicate a decrease in radiance to space, cyan hues an increase. Pixel color intensity indicates the average pixel reflectivity, from the error margin 0.02 (deep blue) to 0.50 (yellow). (**Right**, for channel 10.8 μm) Orange hues mean an increase in the outgoing longwave radiation (OLR), green hues a decrease, with average pixel intensity indicating brightness temperature, from 275 K, in yellow, to 300 K, in black.

The given values for air heating are confirmed by estimates from other data sources, which point to the recent record-low planetary albedo as the primary warming factor [21].

In fact the Sahel Chad basin lately receives increased precipitation, similar to the precipitation during the high phase of the inter-decadal hydrological cycle in 1950-1960 [22,23]. This tallies in our study with the cyan hues in that region. We do not observe a clear pattern in the creation or destruction of cloud in the global MFoV, but an average reduction is clearly the trend.

Several studies [14] point out the prevalence of aerosol trends over greenhouse gas trends in climate warming: "Aerosol reductions significantly contribute to climate warming and increase the frequency and intensity of extreme weathers" [24]. We have not pursued this thesis here.

The relative variation for channel 10.8 μm (Figure 3, right) is not as high as for 0.6 μm, but firmly correlates with the solar decadal variation (Figure 3, left). A Pearson correlation coefficient of 0.71 is noted for the decadal variation in radiances at 0.6μm and 10.8 μm, where a decrease in reflectance at 0.6 μm tends to match an increase in outgoing longwave radiation (OLR) at 10.8 μm. Even the 60 regions we distinguish in Figure 4 show on average that same pattern at the more local scale. Physically a cloud reduction allows an easier escape for heat from the ground. Above the Sahara, mostly cloud free, there is no noticeable change in those two channels.

Figure 4 shows areas of geographical variation in the channel 0.6 μm reflectivity and combinations of radiance values in the infrared or their variation in the decade, namely 10.8 μm and 12.0 μm. A random selection of pixels in each regional square area is represented by color dots indicating their average reflectivity from 3% (in blue) to 60% (in red). We observe there the areas most affected by a decrease in RSW, namely the north Atlantic, eastern Europe, north-east Brazil and off the western coast of southern Africa. On the other hand, the Sahel, central Brazil and areas of the south Atlantic increased their cloud cover, as is also apparent above the warm Agulhas current [25].

 doi:10.20944/preprints202510.2286.v2

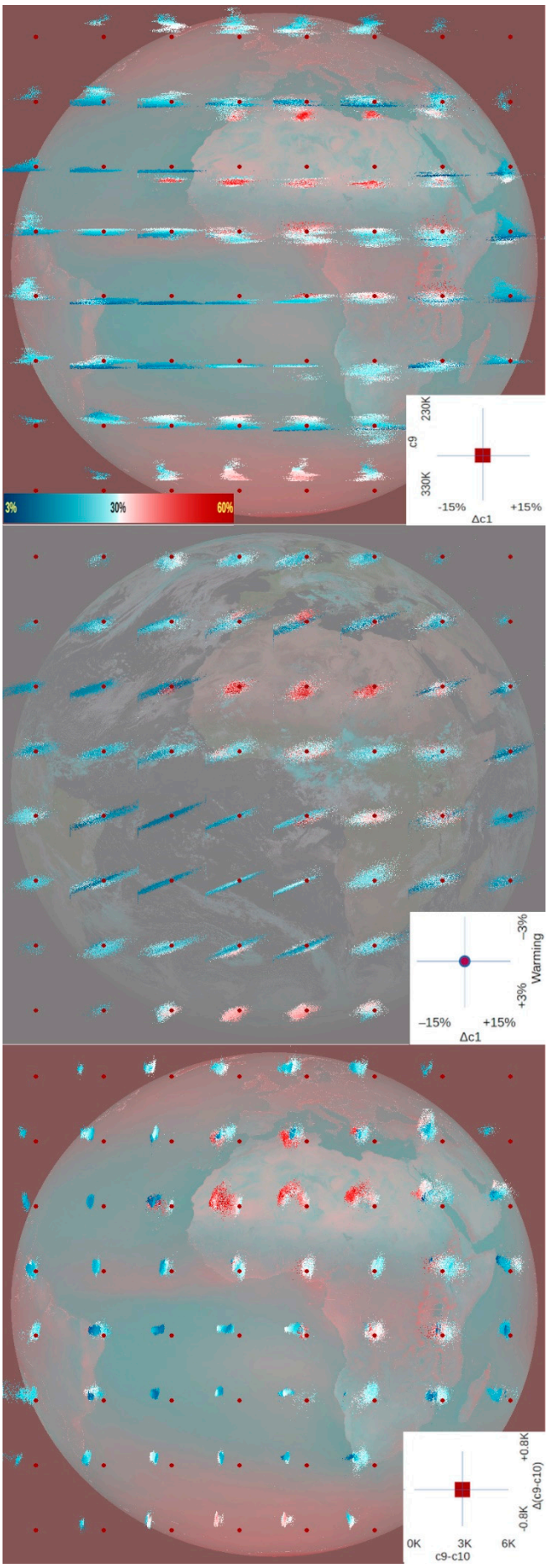

 doi:10.20944/preprints202510.2286.v2

Figure 4. Geographic diagrams of the cloud change. In all three images, pixels are represented by dots in a gradual reflectivity scale from 3% (**blue** dots) to 60% (**red** dots) on the left lower corner. (**Top**) For each of the 60 square regions in which we divided the MFoV, the graph relates average brightness temperature at 10.8 μm in ten years at 12 UTC (vertical axis) with decadal relative change in 0.6 μm reflectivity (horizontal axis), in other words, a heat versus light change. See the inset lower-right corner for the precise limits. For instance, for Mauritania most pixels are very reflective and warm, and tend to lose 0.6 μm radiance in the 'recent' decade. (**Middle**) The regional graph dots again connect the pixel warming or cooling (vertical axis) with the relative variation in reflectivity at 0.6 μm (horizontal). E.g., a vertical value of +1% means a net decadal increase in the imbalance equivalent to 1% of the solar constant. (**Bottom**) Connection of change in the split window (channel 10.8 μm – channel 12.0 μm) brightness temperature difference (vertical) with average difference value in the pixel (horizontal). Graphs background only provided for geographic reference.

3.2. Regional Evolution

Areas with less cloud in the final period than in the initial provide an easier escape route to space for the outgoing longwave radiation. The anomaly correlation for the regional changes in channels 0.6 μm and 10.8 μm is -0.46, and therefore significant, which also shows an intuitive result: with less cloud the Earth is able to release more heat into space, although reducing cloud leads to warming. Areas of increased outgoing longwave radiation (OLR) roughly correlate with areas of decreased reflected shortwave radiation (RSW), but with abundant exceptions. For example, the decrease in low-level cumulus cells hardly affects the OLR, since sea and low cloud have similar emission temperatures.

Desert regions like the Sahara, with scarce cloudiness and marginal land cover transformation, show minimal changes in RSW but considerable variation in OLR over the 20 years. This can be explained by soil temperature increases, but does not exclude aerosol (dust) changes. The Mediterranean area (Figure 4, top) shows a clear decrease in solar reflected radiation for those pixels with lowest reflectivity (sea pixels, blue dots), but little reduction for the land pixels (red dots). Maritime regions like the South Atlantic show high negative correlation between RSW and OLR. In such areas with low presence of human-related aerosols, the registered change must be in the cloud amount. A decrease in the cloud cover optimally explains that less solar radiation is reflected to space (negative RSW), and that more heat from the surface can reach space (positive OLR).

To identify high cloud we counted pixels with particular thresholds in reflectivity and brightness temperatures as follows: Reflectivity at 1.6μm < 25% (ice cloud), at 0.8μm > 90% (bright cloud), brightness temperature (BT) at 10.8μm < 220K (cold cloud) and BT10.8μm – BT12μm < 3K (thick cloud). The number of pixels fulfilling all four conditions is not significantly different in the two decades considered. In this work we disregard the night conditions. The cloud cover decrease concerns mainly the low-level cloud. Warm cloud has a cooling effect on the planet, whereas high-level cloud is typically warming the surroundings, or occasionally having a neutral effect. We have not observed a variation in high-level cloud.

The decadal increase in brightness temperature around 10.8 μm (+0.32 K) and 12.0 μm (+0.20 K) reflect changes in humidity, air temperature, or cloud cover. The difference between these two channels, which has increased by 0.12 K over the decade, is compatible with a (6 ± 2)% rise in specific humidity in the lower atmosphere or with an increase of (0.8 ± 0.2) K in low-level air temperature. A hypothetical decrease of about 6% in high-level cloud cover could also produce a similar differential warming of 0.12 K.

Our analysis on small regions, mainly depicted in Figure 4, shows a high variability among the 60 square regions distinguished within the MFoV in satellite projection, which can be interpreted individually. Red dots in the scatterograms indicate the most reflective pixels in the MFoV on the multi-year average. Blue dots stand for the darkest and are usually linked to clear ocean surfaces.

1. The top image in Figure 4 with inset diagrams shows the pixel connection between the infrared (IR) value of the pixel in kelvin (K) on the vertical axis, and its relative change in 0.6μm radiation on the horizontal. That allows an identification of the temperature of the pixel most affected by

 doi:10.20944/preprints202510.2286.v2

the cloud reduction by just looking at the shift to the left hand side in the dot distribution. For instance, in the north Atlantic west of the Iberian peninsula, it is the warmer pixels suffering dissipation (shift to the left). Off the coast of Namibia, there is a uniform reduction in low level cloud, typically dense fog in convective cells as a result of warm desert air sweeping above the cold Benguela current [26].

2. The middle image in Figure 4 shows pixel estimates by region for the warming due to the decadal change in short and long wave radiation. Blue shades in the scatter plots reveal which cloud level is more influential in the regional warming or cooling. In most regions, it is the most reflecting pixels losing more reflectivity and contributing more to the positive climate imbalance (CI) at the top of the atmosphere. Note that a few values outside of the given boundaries for the horizontal are projected on the vertical axes.
3. The bottom image in Figure 4 shows regional changes for the difference in kelvin between channels at 10.8 μm and at 12.0 μm ('split window difference'), which is globally a growth around 0.2 K in a decade. This increase might well be due to the higher specific humidity in the low levels of the troposphere, as a result of the increase in ocean and land temperatures. We did not find evidence of a general increase in high cloud or thin cirrus, after exploring and counting pixels above particular thresholds defining that cloud. For instance, we used for the check on thick high cloud (HC) two periods of four years (2004–2008, 2019–2023) and counted pixels fulfilling four criteria simultaneously (Figure 4.2):
    a) Reflectivity at 1.6μm < 25% (typical for ice topped cloud)
    b) Reflectivity at 0.8μm > 90% (bright cloud)
    c) Brightness temperature (BT) at 10.8μm < 220K (high thick cloud)
    d) BT 10.8μm – BT 12μm < 3K (thick cloud).

The resulting values of the fraction of pixels (around 6.0×10^{-4}) did not show a difference for the two periods, not even geographically (graph not shown). Pixels occur mainly in the equatorial region around the Gulf of Guinea.

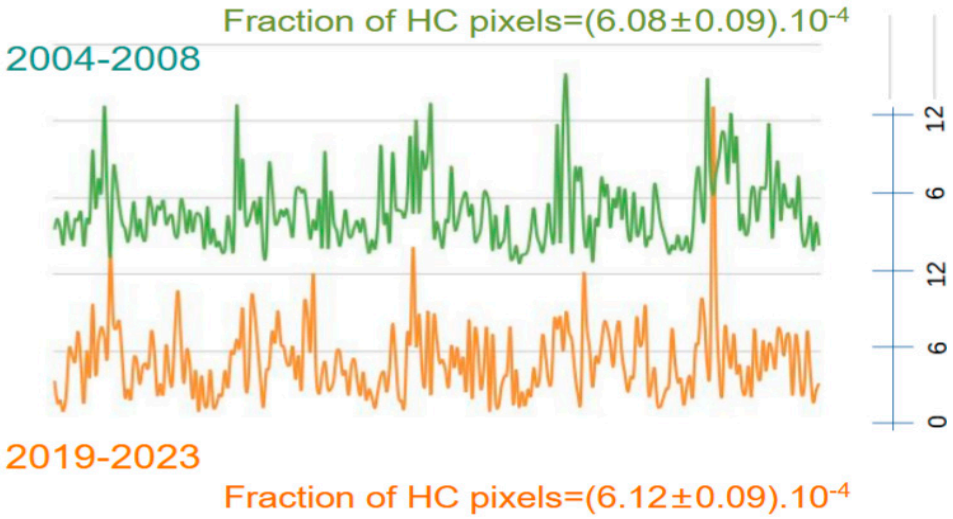

Figure 4.2. Pixel counts in two separate 4-year periods of Meteosat observations, showing no significant change in the presence of thick high cloud (HC) over the MFoV for the evolution in two shorter periods of five years.

4. Over the Sahara we notice a strong variation in the split-window difference, presumably not due to humidity changes, but perhaps to an increase in low-level air temperatures or vegetation in the Sahel region. An increase in greenness over large areas of the Sahel has been measured since the mid-1980s [27a,27b], in correspondence with an increase in cloud in our study (Figure 3, left).

 doi:10.20944/preprints202510.2286.v2

3.3. Sea Surface Temperature (SST)

Using solely Meteosat radiances, we estimate sea surface temperature for every water pixel in the MFoV. Figure 5 provides the overall results for the average and decadal change in SST. The Mediterranean, Black Sea, around Madagascar and the south Seas near Antarctica show the sharpest SST increases. North-west Atlantic and the Caribbean sea show SST cooling.

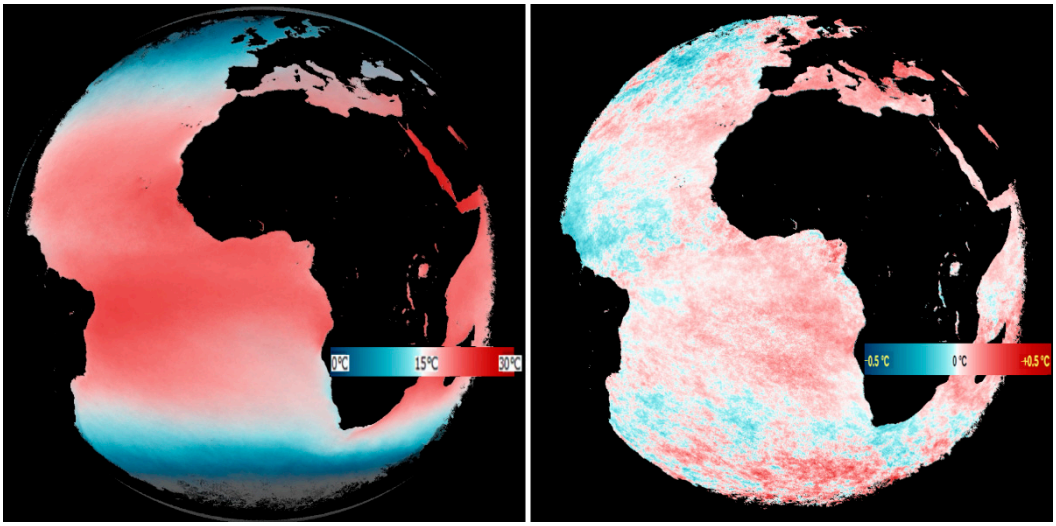

Figure 5. For sea or lake pixels, (**left**) average value in the last decade of the sea surface temperature (SST) at 12 UTC. Equatorial regions show values approaching 30 °C, whereas mid-latitudes are closer to 15 °C in the annual average (**Right**) Change in SST at 12 UTC in a decade, showing a variegated pattern of warmings and coolings, with preponderance of the former. Polar pixels are frequently excluded from the estimate, due to almost permanent cloud.

3.4. Connection of SST and Climate Imbalance

There is a strong connection between the climate imbalance (CI) and the SST change in the monthly time scale (Figure 6A). At the MFoV scale, SST warming occurs approximately between October and February, and cooling during the remaining months. What happens when we eliminate the seasonal variations with a 12-month filter of the imbalance and SST data? Then (Figure 6B) their correlation drops to +0.6 and we observe growth periods in one variable coinciding with level periods in the other. Both variables show a positive trend in the course of the 20 years. The lack of agreement is not surprising, given the complexities of the ocean internal dynamics, which we barely understand. Surface measurements, and float studies on relatively few points, are vastly insufficient for a good comprehension [28].

We do not exclude some influence of El Niño cycles in the Atlantic SST variability. However, both decadal periods under consideration show a similar occurrence of those cycles [4'].

The low cloud reduction, together with the increase in surface and atmosphere temperatures, explains the thermal infrared radiance increase. This result is closely similar to the most recent data from CERES [29], which however shows a smaller change in the absorbed solar radiation. The reason is perhaps that CERES does not cover the last few hot years 2023-2025. Their OLR increase estimate matches ours.

Figure 6.2 offers a comparison of Meteosat SEVIRI and CERES short- and longwave measurements. This is a compelling proof of the lack of spurious trends in Meteosat, given the striking similarity of the series. The averaging of the CERES radiances was chosen with different weights, taking cosine(latitude) as a factor, both latitude and longitude, or no consideration for angles (as in our Meteosat slot averages). The differences in the CERES resulting series varied by less than 2%, and did not significantly affect the Pearson correlation coefficients.

 doi:10.20944/preprints202510.2286.v2

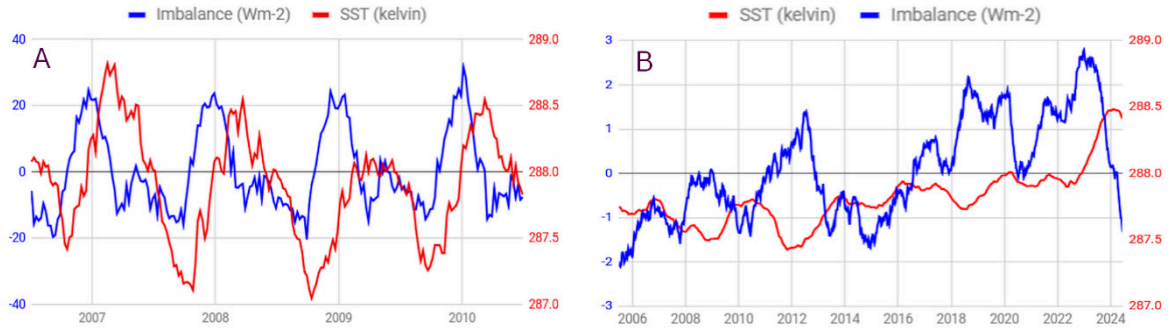

Figure 6. (Left, letter A) Evolution of the climate imbalance (2006-2011) in blue, compared with the SST in the MFoV in red, showing the precise correspondence between the positive phases of the imbalance (from October to February) and the SST growth period, similar for all years. The imbalance leads by ten weeks the average-SST graph in the short term, with Pearson coefficient +0.71 between the two variables. **(Right, letter B)** On a longer time scale (2005-2024) with yearly running-averaged data, the two series display however a weak correlation (+0.42), pointing to ocean dynamics influence. **Note**: At the horizontal axes, the location of the year numeral marks the first week of that year.

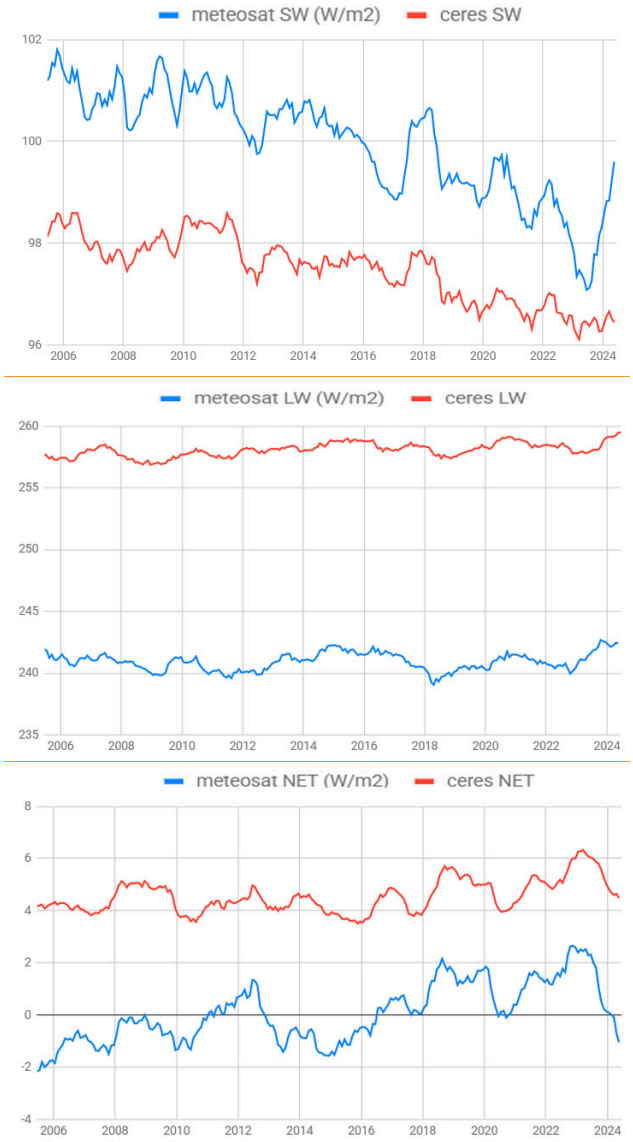

Figure 6.2. Comparison of measurements by CERES and SEVIRI (MSG) instruments both in Wm^{-2}, on the two basic spectral bands, shortwave (solar, **upper** panel) and longwave (thermal infrared, **middle** panel), plus the

 doi:10.20944/preprints202510.2286.v2

net incoming radiance into the Earth system (**lower** panel). Pearson correlations between CERES and SEVIRI are strong, around 0.74 ± 0.07.

The average imbalance during the sea surface warming seasons and the SST variation allows to estimate the mixed layer depth in ca. (35 ± 10) m. That is the layer of turbulence near the sea surface with homogeneous temperature and salinity. This value is an average of north and south Atlantic conditions typically with opposed cycles, smaller than the local yearly amplitudes.

Figure 7 shows the sea surface temperature evolution from January 2020 to June 2025 for different geographic subareas in the MFoV, illustrating a differential warming between the northern hemisphere (NH) and the southern hemisphere (SH) ocean portions. Other recent studies point to this same probable fact, which we have not yet studied in depth [30].

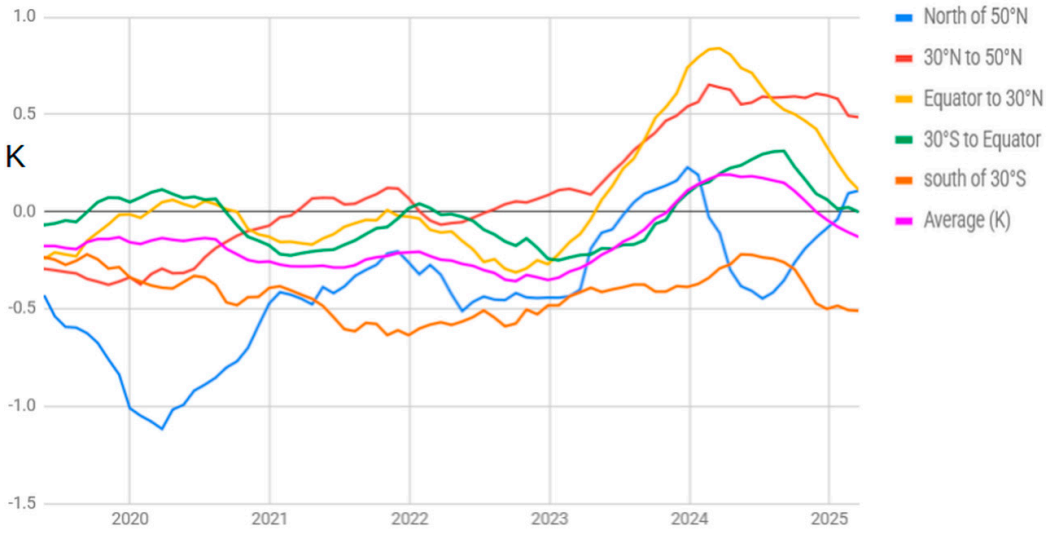

Figure 7. Deseasonalized evolution from July 2020 to February 2025 of the average SST anomaly (in kelvin on the vertical axis) for separate regions within the MFoV, and for the whole Atlantic as seen by Meteosat at 0 degrees ('Average'). The last 12 months' development in the curves shows warming in the high North latitudes and cooling of the tropical waters.

4. Discussion and Conclusions

Our detailed analyses have produced a variety of results, both expected but also sometimes surprising. These we express below, along with suggestions for future investigations.

In response to atmospheric changes in gas and cloud amounts, Meteosat radiances significantly changed between the last two decades of Meteosat data (2005-2024), with marked regional differences, both in the solar and the infrared domains. These changes are much faster and stronger than those due to the slowly drifting total ToA solar irradiance [31].

A low-level cloud decrease affected the Meteosat field of view in these last decades, contributing a large part of the current climate warming, both on land and ocean temperatures, in line with global findings from CERES and ERA-5 [19,29].

The Meteosat ToA imbalance and the CERES net incoming radiation (Figure 6.2) are similar [29], even in their solar and infrared components during the analyzed period for the same geographical frame. We also notice that a comparison of Meteosat and global CERES is almost as good, as if the Atlantic were synchronized with other oceans for the synoptic scale variations. Other estimates ('theirs') are similar to ours, e.g., the change per decade in OLR (–0.27 theirs, –0.30 Wm^{-2} ours), with some divergence in the change of absorbed solar radiation (+0.73 Wm^{-2} theirs, +1.1 Wm^{-2} in our study).

The ocean surface therefore responds quickly to changes in the ToA, but SST does not keep up in pace with the long term (decadal) evolution of the imbalance. This leads to the conclusion that the deep ocean heat accumulation and release to the surface has a strong influence on the SST in the long

 doi:10.20944/preprints202510.2286.v2

term. The deep ocean has an effect on the climate evolution at the surface, which requires new observational data in order to ascertain the phases of absorption and release of heat.

For the period from July 2023 to June 2024 (the most recent year in the moving-averaged data of this study), we observe a significant imbalance reduction mainly due to the solar flux reduction (–3.1 ± 0.5 Wm^{-2}), accompanied by an increase in SST (Figure 6B). This concurrence suggests a largely unknown heat exchange between the boundary layer and the deeper ocean. Some authors [32] estimate that 93% of the imbalance energy ends up in the ocean as heat content (OHC), most noticeable near the surface. We conclude that the SST is an incomplete indicator of ocean heating.

Given the problems around the strong Q branch for CO2 absorption in the IASI OLR product [Whitburn 1'], we dropped any external reference for the current imbalance at the ToA, so that its graph in Figure 6 should not be construed as absolute or confirmed values. In other words, the vertical axis can be shifted in reality. Since imbalance is a weak indicator of the surface temperature rate, we have chosen the zero reference that best explains the accelerating heating in the last few years. The graph's worth lies in showing the imbalance evolution in time, not the imbalance actual values.

The flux imbalance at the top of the atmosphere explains the seasonal cycle changes in the sea surface temperature on the short term. However, there is no response to changes in the ToA imbalance on the sea surface temperatures on the one-year moving averaged series, with poor correlation (+0.35) between SST and imbalance. Mauritzen's suggestion that SST yearly values are "the result of the energy accumulated in earlier years, combined with any rapid change in forcing (e.g., aerosol emissions, volcanic eruptions or solar forcing)" [29] does not get confirmed by our work either. We do not find a time lag which improves the correlation between SST and imbalance. We estimate an Atlantic SST increase of (+0.17 ± 0.05) K in the last ten years, in line with other major sources of climate monitoring [33]. The decadal imbalance growth is at (+0.79 ± 0.15) Wm^{-2}, the sum of all spectral terms in Table 2, according to Meteosat data. These two values match a spread of the imbalance heat in the upper ocean layer of 170 m, which is close to a rough estimate of the oceans boundary layer depth.

The imbalance flux guides the short term evolution of the SST, but not the long term, allowing time for part of its power to warm deeper layers of the ocean through incompletely studied mechanisms [34].

Several researchers trace the albedo reduction back to a loss of cloud (and ice or snow in areas outside the MFoV) and to legal aerosol limits as causes of warming [35]. They mention a "possibly emerging low-cloud feedback", which affects the climate projections. Our work supports that low-cloud is not only affecting the climate warming, but also appears to have been its main driver in the last decade, though not precluding different future influences or trends.

Figures 4 and 5 show the lack of connection between the two climate variables cloudiness and SST. Whereas the region north of the Venezuelan coast shows SST cooling and cloud loss at all levels, the portion of Indian Ocean included in the MFoV shows an increase of SST under a similar cloud loss. We do not find a strong correlation of cloud change and ToA imbalance in any region. A similar lack of correlation also applies to the globally averaged 10.8-μm radiance and imbalance. There is however a weak correlation between the MFoV total SST and ToA imbalance (Pearson = +0.41) [35].

The deep ocean requires urgent exploration in order to ascertain the role of internal dynamics in changes on SST, which cannot be traced back to the ToA imbalance alone. The massive amount of water contained in Earth's oceans is a major driver of our planet's climate. The relevance of understanding its dynamics and influences cannot be over-emphasized.

Author Contributions: Conceptualization, J.P.; methodology, J.P.; software, J.P.; validation, H.B. and J.P.; formal analysis, J.P. and H.B.; investigation, J.P. and H.B.; resources, H.B. and J.P.; data curation, J.P.; writing—original draft preparation, J.P. and H.B.; writing—review and editing, H.B. and J.P.; visualization, J.P. and H.B.; funding acquisition, H.B. All authors have read and agreed to the published version of the manuscript.

Funding: This research was partially funded by budget funds from the Federal University of Alagoas.

 doi:10.20944/preprints202510.2286.v2

Data Availability Statement: https://user.eumetsat.int.

Acknowledgments: This study uses as the main data source the Meteosat store from EUMETSAT, the European Organization for the Exploitation of Meteorological Satellites. Thanks are due to Richard Swifte for his selfless contribution to improve the text and his valuable comments. Thanks also to Dr. Tim Hewison for his advice and expertise regarding the calibration of Meteosat.

Conflicts of Interest: The authors declare no conflict of interest. The funders had no role in the design of the study; in the collection, analyses, or interpretation of data, in the writing of the manuscript, or in the decision to publish the results.

References

1'. DOI: Spectrally resolved fluxes ... Whitburn S. et al. https://doi.org/10.1175/JCLI-D-19-0523.1
2'. on aerosols: Paulot, F., D. Paynter, P. Ginoux, V. Naik, L. W. Horowitz, 2018: Changes in the aerosol direct radiative forcing from 2001 to 2015: observational constraints and regional mechanisms. Atmos. Chem. Phys., 18(17), 13265-13281 . doi: 10.5194/acp-18-13265-2018.
3'. Expand for standard reference number 15 below!!!!!!!!!!!!!
4'. Ineson, S., Scaife, A. The role of the stratosphere in the European climate response to El Niño. *Nature Geosci* 2, 32–36 (2009). https://doi.org/10.1038/ngeo381
1. Dewitte, S.; Nevens, S. Earth's radiation budget from 1979 to present derived from satellite observations. Copernicus Climate Change Service (C3S) Climate Data Store (CDS). 2021. https://doi.org/10.24381/cds.85a8f66e (accessed on 5 August 2025)
2. Xu, JL; Liang, SL; Jiang, B. A global long-term (1981-2019) daily land surface radiation budget product from AVHRR satellite data using a residual convolutional neural network. Earth System Science Data 2022, 14(5), 2315-2341.
3. Gupta, S. K.; Ritchey, N. A.; Wilber, A. C.; Whitlock, C. H.; Gibson, G. G.; Stackhouse, P. W. A Climatology of Surface Radiation Budget Derived from Satellite Data. J. Climate 1999, 12(8), 2691-2710. https://doi.org/10.1175/1520-0442(1999)012<2691:ACOSRB>2.0.CO;2
4. Payez, A.; Dewitte, S.; Clerbaux, N. Dual View on Clear-Sky Top-of-Atmosphere Albedos from Meteosat Second Generation Satellites. Remote Sens. 2021, 13, 1655. https://doi.org/10.3390/rs13091655.
5. Bojinski, S.; Verstraete, M.; Peterson, T.C.; Richter, C.; Simmons, A.; Zemp, M. The Concept of Essential Climate Variables in Support of Climate Research, Applications, and Policy. Bull. Am. Meteorol. Soc. 2014, 95, 1431–1443.
6. Schmetz, J.; Pili, P.; Tjemkes, S.; Just, D.; Kerkmann, J.; Rota, S.; Ratier, A. An Introduction to Meteosat Second Generation (MSG). Bull. Am. Meteorol. Soc. 2002, 83, 977–992.
7. Harries, J.E.; Russell, J.E.; Hanafin, J.A.; Brindley, H.; Futyan, J.; Rufus, J.; Kellock, S.; Matthews, G.; Wrigley, R.; Last, A.; et al. The Geostationary Earth Radiation Budget Project. Bull. Am. Meteorol. Soc. 2005, 86, 945–960.
8. Harries, J. E., H. E. Brindley, P. J. Sagoo, and R. J. Bantges, 2001: Increases in greenhouse forcing inferred from the outgoing longwave radiation spectra of the Earth in 1970 and 1997. Nature, 410, 355-357
9. Meirink, J.F., R.A. Roebeling and P. Stammes, 2013: Inter-calibration of polar imager solar channels using SEVIRI, Atm. Meas. Tech., 6, 2495-2508, doi:10.5194/amt-6-2495-2013
10. T. J. Hewison *et al.*, "GSICS Inter-Calibration of Infrared Channels of Geostationary Imagers Using Metop/IASI," in *IEEE Transactions on Geoscience and Remote Sensing*, vol. 51, no. 3, pp. 1160-1170, March 2013, doi: 10.1109/TGRS.2013.2238544.
11. Brindley, H.E.; Bantges, R.J. The Spectral Signature of Recent Climate Change. Curr Clim Change Rep. 2016, 2, 112–126. https://doi.org/10.1007/s40641-016-0039-5
12. Samset, B.H., Zhou, C., Fuglestvedt, J.S. *et al.* Steady global surface warming from 1973 to 2022 but increased warming rate after 1990. *Commun Earth Environ* 4, 400 (2023). https://doi.org/10.1038/s43247-023-01061-4

13. Fernández, J. I. P., & Georgiev, C. G. (2023). *Evolution of Meteosat Solar and Infrared Spectra (2004–2022) and Related Atmospheric and Earth Surface Physical Properties. Atmosphere, 14*(9), 1354. https://doi.org/10.3390/atmos14091354
14. Armour, K; Collins, W.; Dufresne, J-L.; Frame, D.; Lunt, D.J.; Mauritsen, T.; Palmer, M.D.; Watanab, M.; Wild, M.; Zhang, H. et al. The Earth's Energy Budget, Climate Feedbacks, and Climate Sensitivity. In IPCC Sixth Assessment Report. Working Group 1; Forster, P., Storelvmo, T., Coord. Authors; WMO; UNEP: Geneva, Switzerland, 2007. https://www.ipcc.ch/report/ar6/wg1/chapter/chapter-7/. (accessed on 25 June 2023)
15. https://journals.ametsoc.org/view/journals/clim/22/3/2008jcli2637.1.xml EXPAND for PROPER REFERENCE!!!
16. Copernicus Climate Change Service (C3S). (2025, April 15). *Climate indicators: Ocean heat content.* Retrieved October 18, 2025, from https://climate.copernicus.eu/climate-indicators/ocean-heat-content
17. Kidder, S.Q.; von der Haar, T. H. *Satellite meteorology, An introduction*. Academic Press, 1995; 466 pp.
18. Rohde, R. Global Temperature Report for 2024. Berkeley Earth, U.S. non-profit organization focused on environmental data science and analysis. Available online: https://berkeleyearth.org/global-temperature-report-for-2024/.
19. Zhang, Y; Jeevanjee, N; Fueglistaler, S. Linearity of Outgoing Longwave Radiation: From an Atmospheric Column to Global Climate Models. https://doi.org/10.1029/2020GL089235
20. Jing Feng *et al* 2023: How atmospheric humidity drives the outgoing longwave radiation–surface temperature relationship and inter-model spread, *Environ. Res. Lett.* 18 104033 doi:10.1088/1748-9326/acfb98
21. Goessling, H. F., Rackow, T., & Jung, T. (2024). Recent global temperature surge amplified by record-low planetary albedo. *Science, 384*(6693), 66–70. https://doi.org/10.1126/science.adq7280
22. Salack, S., Giannini, A., & Sarr, B. (2016). Rainfall trends in the African Sahel: Characteristics, processes, and causes. *Wiley Interdisciplinary Reviews: Climate Change, 7*(3), 367–388. https://doi.org/10.1002/wcc.591
23. Odoulami, R. C., et al. (2024). Strengthening of the hydrological cycle in the Chad Basin. *Scientific Reports, 14*, Article 75707. https://www.nature.com/articles/s41598-024-75707-4
24. https://www.nature.com/articles/s41467-023-42891-2. Aerosols overtake greenhouse gases causing a warmer climate and more weather extremes toward carbon neutrality. Pinya Wang, Yang Yang et al.
25. Stramma, L., Cornillon, P., Weller, R. A., & Price, J. F. (1997). Observations of Agulhas Current variability. *Journal of Geophysical Research: Oceans, 102*(C3), 5513–5523. https://oceanrep.geomar.de/id/eprint/6196/
26. Shannon, L. V., & Nelson, G. (1996). The Benguela: Large-scale features and processes and system variability. In A. R. Robinson & K. H. Brink (Eds.), *The Sea* (Vol. 11, pp. 163–210). https://www.sciencedirect.com/science/article/abs/pii/S0079661109001104
27. a. Olsson, L.; Eklundh, L.; Ardö, J. A recent greening of the Sahel—trends, patterns and potential causes. *Atmosphere* 2005, *63*, 556–566. https://doi.org/10.1016/j.jaridenv.2005.03.008. b. Herrmann, S.M.; Anyamba, A.; Tucker, C.J. Recent trends in vegetation dynamics in the African Sahel and their relationship to climate. *Glob. Environ. Change* 2005, *15*, 394–404. https://doi.org/10.1016/j.gloenvcha.2005.08.004
28. Roemmich, D., et al. (2023). Observing the full ocean volume using Deep Argo floats. *Frontiers in Marine Science, 10*, 1287867. https://doi.org/10.3389/fmars.2023.1287867
29. Mauritsen, T., Tsushima, Y., Meyssignac, B., Loeb, N. G., Hakuba et al. (2025). Earth's energy imbalance more than doubled in recent decades. *AGU Advances, 6*(3), Article e2024AV001636. https://doi.org/10.1029/2024AV001636
30. Loeb, N. G., Thorsen, T. J., Kato, S., Rose, F. G., Hodnebrog, Ø., & Myhre, G. (2025). Emerging hemispheric asymmetry of Earth's radiation. *Proceedings of the National Academy of Sciences of the United States of America, 122*(40). https://doi.org/10.1073/pnas.2511595122
31. Chatzistergos, T., Krivova, N. A., & Yeo, K. L. (2023). *Long-term changes in solar activity and irradiance. Journal of Atmospheric and Solar-Terrestrial Physics, 252*, 106150. https://doi.org/10.1016/j.jastp.2023.106150
32. Cheng, L., Abraham, J., Hausfather, Z., & Trenberth, K. E. (2019). *How fast are the oceans warming? Science, 363*(6423), 128–129. https://doi.org/10.1126/science.aav7619

 doi:10.20944/preprints202510.2286.v2

33. Berkeley Earth. (2025, July 11). Temperature update for June 2025: Third warmest June in the instrumental record. *Berkeley Earth*. Retrieved from https://berkeleyearth.org/june-2025-temperature-update/
34. Gutjahr, O., et al. (2021). *Comparison of ocean vertical mixing schemes in the MPI-ESM1.2.* Geoscientific Model Development, 14, 2317–2349